Measuring and modelling investigation of the Net Photochemical Ozone Production Rate via an improved dual-channel reaction chamber technique

Yixin Hao[1,2#], Jun Zhou[1,2#*], Jieping Zhou[1,2], Yan Wang[1,2], Suxia Yang[1,2], Yibo Huangfu[1,2], Xiaobing Li[1,2], Chunsheng Zhang[3], Aiming Liu[3], Yanfeng Wu[1,2], Shuchun Yang[1,2], Yuwen Peng[1,2], Jipeng Qi[1,2], Xianjun He[1,2], Xin Song[1,2], Yubin Chen[1,2], Bin Yuan[1,2*], Min Shao[1,2]

[1]Institute for Environmental and Climate Research, Jinan University, Guangzhou 511443, China

[2]Guangdong-Hongkong-Macau Joint Laboratory of Collaborative Innovation for Environmental Quality, Guangzhou 511443, China

[3]Shenzhen National Climate Observatory, Shenzhen 518040, China

[#]Yixin Hao and Jun Zhou contribute equally to this work.

Correspondence to: Jun Zhou (Junzhou@jnu.edu.cn) and Bin Yuan (byuan@jnu.edu.cn)

Abstract. Current process-based research mainly used the box model to evaluate the photochemical ozone production and destruction rates, it is not clear to which extend the photochemical reaction mechanisms were understood. Here, we modified and improved a net photochemical ozone production rate (NPOPR, $P(O_3)_{net}$) detection system based on current dual-channel reaction chamber technique, which make the instrument appliable to different ambient environment, and its various operating indicators were characterized, i.e., the airtightness, light transmittance, wall losses of the reaction and reference chambers, conversion rate of O_3 to NO_2, the air residence time, and the performance of the reaction and reference chambers, etc. The limit of detection of NPOPR detection system were determined as 0.07, 1.4, and 2.3 ppbv h^{-1}, at the sampling flow rates of 1.3, 3, and 5 L min^{-1}, respectively. We further applied NPOPR detection system in the field observation at an urban site at Pearl River Delta (China). During the observation period, the maximum value of $P(O_3)_{net}$ was 34.1 ppbv h^{-1}, which was ～ 0 ppbv h^{-1} at night within the system detection error and peaks at around noon local time, the daytime (from 6:00–18:00) average value of $P(O_3)_{net}$ was 12.8 ($\pm$5.5) ppbv h^{-1}. We investigated the detailed photochemical O_3 formation mechanism in the reaction and reference chambers of NPOPR detection system using a zero-dimensional box model. We found that the photochemical reactions in the reaction chamber were very close to that in the ambient air, but it was not zero-chemistry in the reference chamber, on the contrary, the reaction related to the production and destruction of RO_2 (=HO_2+RO_2) continues in

33   the reference chamber, which led to small amount of $P(O_3)$net. Therefore, the $P(O_3)$net measured here

34   can be regarded as the lower limit of the real $P(O_3)$net in the atmosphere, however, the measured $P(O_3)_{net}$

35   were still ~ 7.5 ppbv h^{-1} to 9.3 ppbv h^{-1} higher than the modeled $P(O_3)_{net}$ value depending on different

36   modeling methods, this may be due to the inaccurate estimation of HO_2/RO_2 radicals in the modeling

37   study. Short-lived intermediates measurements coupling with direct $P(O_3)_{net}$ measurements are needed

38   in future in order to understand the O_3 photochemistry better. Our results show that the NPOPR detection

39   system can achieve high time resolution and continuous field observation, which helps us to understand

40   photochemical O_3 formation better and provides a key scientific basis for the continuous improvement

41   of air quality in China.

42

43

44 **1 Introduction**

45 Surface O_3 pollution has become a major challenge in air quality management in China (Shen et al.,

46 2021). Elevated surface O_3 concentrations exert severe adverse effects on public health, such as

47 respiratory diseases, and the estimated annual mortality attributable to surface O_3 exposure is over

48 150,000 deaths in China (Malley et al., 2017). O_3 pollution is also detrimental to key staple crop yields,

49 reducing the yields of wheat, soybean, and maize by up to 15 %, and is threatening global food security

50 (Avnery et al., 2011; Mills et al., 2018; Karakatsani et al., 2010; Berman et al., 2012; O'Neill et al., 2003).

51 As a greenhouse gas, O_3 also contributes significantly to climate change (Bell et al., 2004). With the

52 rapid economic development and urbanization in the Pearl River Delta (PRD) region in China, O_3

53 pollution is pretty severe, especially in summer and autumn (Zou et al., 2015; Zhang et al., 2021).

54 The variation of O_3 in the planetary boundary layer is predominantly influenced by deposition,

55 advection transport, vertical mixing, meteorological factors, and chemical reactions. Therefore, the O_3

56 budget in the boundary layer can be expressed as Eq. (1) (Sadanaga et al., 2017; Cazorla et al., 2010).

57
$$\frac{\partial [O_3]}{\partial t} = \underbrace{P(O_3) - D(O_3)}_{P(O_3)_{net}} - \underbrace{\frac{v}{H}[O_3]}_{SD} + \underbrace{u_i \frac{\partial [O_3]}{\partial x_i}}_{A} \tag{1}$$

58 $\qquad\qquad P(O_3)_{net} \qquad SD \qquad A$

59 where $[O_3]$ is the ambient O_3 concentration, $P(O_3)_{net}$, $P(O_3)$, and $D(O_3)$ are the net chemical production

60 rate, chemical O_3 production rate, and O_3 chemical loss rate, respectively; SD, v, H, u_i and A represent

61 surface deposition, O_3 deposition velocity, mixing layer height, velocity in three directions and advection

62 consisting of the u_i times the O_3 gradient in those three directions.

63 Tropospheric O_3 is a key component of photochemical smog, mainly formed by photochemical

64 reactions of nitrogen oxides ($NO_x=NO+NO_2$) and volatile organic compounds (VOCs) (Lee et al., 2010).

65 The specific process of the photochemical reaction is the photolysis of NO_2 at 424 nm to generate $O(^3P)$

66 atoms, thereby promoting the formation of O_3. Simultaneously, there is a RO_X ($RO_X =OH + HO_2 +RO_2$)

67 radical cycle in the troposphere, which continuously provides HO_2 and RO_2 to oxidize NO to NO_2

68 resulting in the accumulation of O_3 (Shen et al., 2021; Sadanaga et al., 2017; Cazorla et al., 2010).

69 Typical meteorological scenarios for the occurrence of O_3 pollution episodes in polluted urban

70 centers are usually characterized by weak winds, strong solar radiation, and high temperature (T). Under

71 such conditions, local formation of O_3 plays a crucial role in the rapid increase of surface O_3 in daytime.

72   In addition, in Eq. (1), the surface deposition and advection of O_3 are proportional to ambient O_3

73   concentration [O_3], which is mainly generated by local photochemistry. If $P(O_3)_{net}$ can be reduced by

74   regulatory measures, overall O_3 levels will decline proportionately over time (Cazorla et al., 2010), thus,

75   the investigation of $P(O_3)_{net}$ formation mechanism is urgently needed.

76   Current studies on $P(O_3)_{net}$ estimation mainly rely on modeling methods, the gas-phase chemical

77   mechanisms were frequently used to identify key drivers of O_3 pollution events and provide guidance for

78   making effective O_3 reduction strategies, such as the Master Chemical Mechanism (MCM), the regional

79   atmospheric chemistry mechanism (RACM), the Carbon Bond mechanisms (CBM) and the Mainz

80   Organic Mechanism (MOM) (Shen et al., 2021; Kanaya et al., 2016; Wang et al., 2014; Tadic et al.,

81   2020; Ren et al., 2013; Lu et al., 2010; Zhou et al., 2014; Mazzuca et al., 2016). However, uncertainties

82   in emission inventories, chemical mechanisms, and meteorology make it difficult to perfectly reproduce

83   real atmospheric processes, which can lead some bias in modeling the $P(O_3)_{net}$. According to the existing

84   field observations, researchers found that the concentration of HO_2 or RO_2 obtained from the model

85   simulation was inconsistent with that obtained from the direct measurement, leading to the deviation of

86    $P(O_3)_{net}$ between observation and model simulation results (Wang et al., 2014; Tadic et al., 2020; Ren et

87   al., 2013; Martinez et al., 2003). Therefore, we urgently need a method that can directly measure the

88    $P(O_3)_{net}$.

89   Recently, researchers have developed sensors that can directly measure $P(O_3)_{net}$ in the atmosphere

90   using the dual-channel chamber technique (Sadanaga et al., 2017; Cazorla et al., 2010; Baier et al., 2021;

91   Sklaveniti et al., 2018), where ambient air is introduced into two chambers of identical size, one UV

92   transparent chamber (reaction chamber) and one UV protection chamber (reference chamber). In the

93   presence of solar UV light, O_3 is produced by photochemical reactions in the reaction chamber, but not

94   in the reference chamber. The system does not directly measure O_3 concentrations, it measures the

95   combined concentration of O_3 and nitrogen dioxide (NO_2). $P(O_3)_{net}$ is determined by the difference of

96    $O_X(O_X=O_3+NO_2)$ concentration between the reaction and reference chambers. These studies have greatly

97   helped us to understand the O_3 photochemical formation mechanism, but defects still exists in current

98   studies, for example, the sensors developed by Cazorla et al. (2010) and Baier et al. (2021) both have an

99   NO_2-to-O_3 converter unit, and uses a modified O_3 monitor (Thermo Scientific, Model 49i, USA) to

100   measure Ox, but the zero point of the O_3 monitor is easy to drift, together with the limitation of the

101 conversion efficiency of NO_2 to O_3 (~ 99.9 %) and the effects of the T and relative humidity (RH) to O_3

102 monitor, this method can introduce large measurement uncertainties. Sklaveniti et al. (2018) have shorten

103 the average residence time in the chambers to 4.5 minutes, which reduced the scattering and increased

104 the time resolution of ΔOx measurement, but large wall loss still exists in their system, which are 5 %

105 and 3 % for O_3 and NO_2, respectively. Sadanaga et al. (2017) passed the NO standard gas into the PFA

106 tube to convert O_3 into NO_2 to detect Ox, which is easy to operate, but the LIF-NO_2 detector is less

107 portable and maintainable. Furthermore, all the current sensors have different degrees of NO_2 and O_3 that

108 can even reach 15 %, which largely affect the accuracy of the evaluation of $P(O_3)_{net}$.

109   In this study, we modified and improved the $P(O_3)_{net}$ sensor based on the dual-channel technique

110 as described above and named it as a net photochemical ozone production rate (NPOPR) detection system.

111 The improvement and characterization of the NPOPR detection system are described in Sect. 2.

112 Furthermore, we applied the NPOPR detection system to the observation campaign conducted at

113 Shenzhen Meteorological Gradient Tower (SZMGT) in PRD region in China. A zero-dimensional box

114 model based on the Framework for 0-D Atmospheric Modeling (F0AM) v3.2 coupled with MCM v3.3.1

115 was used to simulate the photochemical reactions inside both the reaction and reference chambers in the

116 NPOPR system, which make us be able to access the ability of the current modeling method to model

117 $P(O_3)_{net}$, as described in Sect. 3. The current research can help us to study the source and formation

118 mechanism of O_3, and provide effective theoretical support for the prevention and control of O_3 pollution.

119 Since the system can directly obtain real-time $P(O_3)_{net}$ under different environmental conditions, it can

120 meet richer and more specific research needs.

121 **2 Method and materials**

122 **2.1 Development of the NPOPR detection system**

123 The schematic and actual diagram of the NPOPR detection system are shown in Fig. 1, the integral

124 construction is similar to the P-L(Ox) measurement system built by Sadanaga et al. (2017) and Sklaveniti

125 et al. (2018), which mainly consists the reaction and reference chambers with the same geometry and

126 made of quartz (190.5 mm inner diameter and 700 mm length, more details can be found in Fig. S1). In

127 order to prevent photochemical reactions inside the reference chamber, a UV protection film (SH2CLAR,

128 3M, Japan) is used to cover the outer surface of it to block the sunlight with the wavelengths < 390 nm.

129   During the experiment, both reaction and reference chambers are located outdoors, exposing to the

130   sunlight directly to simulate the genuine ambient photochemistry reactions, ambient air are introduced

131   into the reaction and reference chambers with the same flow rate, a Teflon filter was amounted before

132   the chamber inlet to remove fine particles. A stream of the air from the two chambers is alternately

133   introduced into a NO-reaction chamber every 2 minutes to covert O_3 in the air to NO_2 in the presence of

134   a high concentrations of NO ($O_3+NO=NO_2$), and the Ox concentrations from the outlet NO-reaction

135   chamber, i.e., the total NO_2 concentration including the inherent NO_2 in the ambient and that converted

136   from O_3 is measured by a Cavity Attenuated Phase Shift (CAPS) NO_2 Monitor (Aerodyne research, Inc.,

137   Billerica MA, USA), in order to avoid other nitrogen oxides interferences to the NO_2 measurement (such

138   as alkyl nitrates, peroxyacyl nitrates, peroxynitric acid, nitrogen pentoxide, etc.). Compared to previous

139   studies which use a dual-channel UV-absorption O_3 monitor (Cazorla et al., 2010) or the LIF-NO_2

140   monitor (Sadanaga et al., 2017) for the Ox measurements, our choice could make the NPOPR detection

141   system has more stable zero base line and more portable. Additionally, we modified the air sampling

142   system to adjust the total air flow rates freely from 1.3 to 5 L min^{-1} in the reaction and reference chambers,

143   which enable us to achieve different air residence time from 3.8 to 21 minutes, this time range covered

144   all the residence time from previous studies using different Ox measurement techniques, which ranged

145   from 4.5 to 20.5 minutes (Cazorla et al., 2010; Baier et al., 2015; Sadanaga et al., 2017; Sklaveniti et al.,

146   2018). According to the simulation results described in Sect. 3, the reaction rates of O_3 formation and

147   destruction pathways and the radicals that play critical roles in photochemical O_3 formation, such as HO_2,

148   RO_2 and OH, reached quasi-steady states in about 3 minutes, so it is reasonable for us to set the air flow

149   rate highest at 5 L min^{-1}, where the sampled air have already reacted for 3.8 minutes in the reaction and

150   reference chambers. On the other hand, this also demonstrated that it is reasonable to set the alternate

151   sampling time for the reaction and reference chambers at 2 minutes, where the sampled air actually have

152   already reacted for at least 3.8 minutes in the reaction and reference chambers. The switch system was

153   controlled by two Teflon three-way solenoid valves (001-0028-900, Parker, GER) located before the NO-

154   reaction chamber (see Fig. 1). To keep the flow rates in the reaction and reference chambers always the

155   same and avoid the gas flow accumulation in the chamber, a pump (pump 3) is connected to the Teflon

156   three-way solenoid valves in parallel to NO-reaction chamber to evacuate the air that is not introduced

157   into the NO-reaction chamber. To reduce NO interference, the system uses O_X to infer the amount of O_3

158   generated by photochemical reactions (Liu et al., 1977; Pan et al., 2015; Lu et al., 2010). The difference

159   of Ox concentrations in the reaction and reference chambers, denoted by ΔOx, represents the amount of

160   O_3 generated by photochemical reaction. $P(O_3)_{net}$ was obtained by dividing ΔOx by the average residence

161   time of air in the reaction chamber $\langle \tau \rangle$:

162    $$P(O_3)\text{net} = P(O_x) = \frac{\Delta O_x}{\tau} = \frac{[O_x]_{reaction} - [O_x]_{reference}}{\tau}$$ (2)
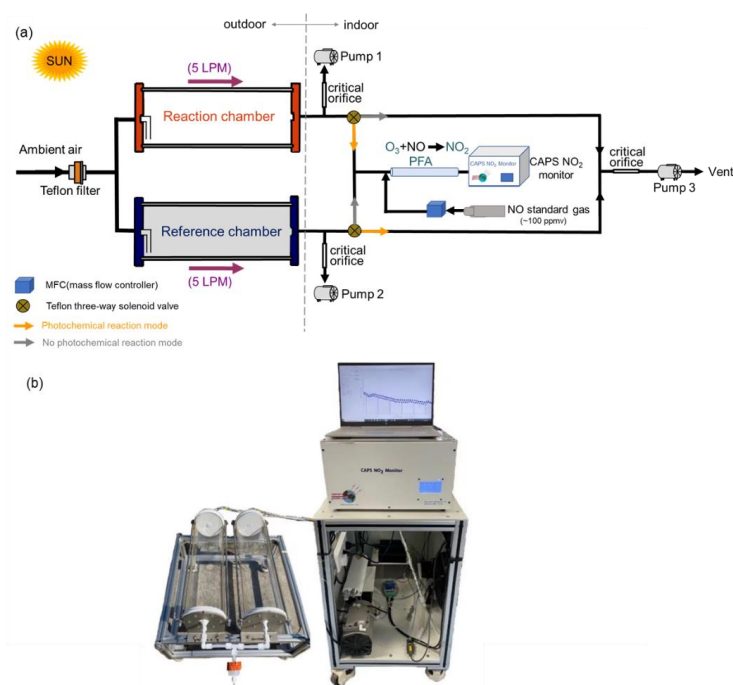
163

164   **Figure 1: (a) Schematic and (b) actual diagram of the NPOPR detection system.**

165   The major improvements of NPOPR detection system described here compared to previous studies

166   to optimize the $P(O_3)_{net}$ measurements were as follows: (1) we improved the design of the reaction and

167   reference chambers to make sure they have good airtightness, this will increase the measurement

168   accuracy of different species inside the chambers, more details can be found in Sect. 2.2 and Sect. S1;

169   (2) added two pumps (labeled as pump 1 and pump 2 in Fig.1) directly after the reaction and reference

170   chambers to continuously draw ambient air through the two chambers (as the makeup flow) to adjust the

171   total air flow rates freely from 1.3 to 5 L min^{-1} in the chambers, by doing this, we are able to achieve

172   different limit of detection (LOD) of NPOPR system (see Sect. 2.4), which make the instrument appliable

173   to different ambient environment, i.e., at high polluted area, we could use higher air flow rates to reduce

174   the wall loss effects of the chambers, at less polluted area, we could use lower flow rates to increase the

175   instrument LOD; (3) accordingly, we characterized the NPOPR detection system at different air flow

176   rates (including 1.3, 2, 3, 4, and 5 L min^{-1}), and tested the conversion efficiency of O_3 by NO to NO_2 in

177   the NO-reaction chamber at different NO concentrations and NO-reaction chamber lengths, all these

178   efforts enable us to understand the running parameters of NPOPR system better and do the data

179   corrections when NPOPR is operated at different air flow rates (see Sect. 2.2); (4) we tested the

180   performance of both reaction and reference chambers by combining the field measurement and the MCM

181   modelling method, which indicated that reaction pathways of $P(O_3)$ and $D(O_3)$ and the radicals that play

182   critical roles in photochemical O_3 formation, such as HO_2, RO_2 and OH, reached quasi-steady states

183   in about 3 minutes, thus make sure that the lowest air residence time at 3.8 min (at air flow rate of

184   5 L min^{-1}) in the reaction and reference chambers is long enough to obtain the accurate $P(O_3)_{net}$

185   values (see Sect. 3.2). By doing the above-mentioned efforts, we were able to make the NPOPR system

186   work more accurately and widely used.

187   **2.2 Characterization of the NPOPR detection system**

188   We characterized the NPOPR detection system following the same procedures as the previous researchers

189   have been done, including the residence time of the air, the wall losses of NO_2 and O_3, and the

190   transmittance of the light in the reaction and reference chambers, as well as the quantitative conversion

191   efficiency of O_3 to NO_2 (α) in the NO-reaction chamber. Additionally, we have investigated the residence

192   time of the air and the wall losses of NO_2 and O_3 in the reaction and reference chambers at different flow

193   rates (including 1.3, 2, 3, 4, and 5 L min^{-1}), and the conversion efficiency of O_3 by NO to NO_2 in the NO-

194   reaction chamber at different NO concentrations and NO-reaction chamber lengths. The detailed

195   experimental performances and data analysis are shown in the supplement (Sect. S1), the corresponding

196   results are described as follows.

197   *The residence time.* We tested the residence time of air in both chambers under different air flow

198   rates, including 1.3, 2, 3, 4, and 5 L min^{-1}, the obtained related residence time in the reaction chamber

199   were 0.35, 0.16, 0.11, 0.07, and 0.06 h, respectively. By setting different air flow rates, we were able to

200   obtain different residence time thus different limit of detection of NPOPR system, which make it

201   applicable to different ambient environment. To make sure that the mean residence time of air is the same

202 in the reaction and reference chambers, we also tested the residence time of air in the reference chamber

203 in parallel, which were not much difference with that in the reaction chamber, as shown in Table S1. The

204 experimental schematic diagram is shown in Fig. S2, the related results of different air flow rates are

205 shown in Figs. S3 and Table S1.

206 ***The wall losses of NO₂ and O₃.*** At the air flow rates of 1.3, 2, 3, 4, and 5 L min⁻¹, the wall losses

207 of O_3 in the reaction chamber were found to be approximately 2 %, 0 %, 0 %, 0 %, and 0 %, respectively,

208 the wall losses of O_3 in the reference chamber was found to be approximately 2 %, 1 %, 1 %, 0%, and

209 0.7 %, respectively. While the wall losses of NO_2 in the reaction chamber at the air flow rates of 1.3, 2,

210 3, 4, and 5 L min⁻¹ were found to be approximately 4 %, 4 %, 2 %, 0%, and 0.3 %, respectively, the wall

211 losses of NO_2 in the reference chamber were found to be approximately 2 %, 1 %, 0 %, 0 %, and 0.6 %,

212 respectively. The experimental schematic diagram is shown in Fig. S4, the related results of different air

213 flow rates are shown in Figs. S5 and Table S2. We further compared the wall losses of O_3 and NO_2 in the

214 reaction and reference chambers at 5 L min⁻¹ with previous studies (as shown in Table S3), and found

215 they were significantly smaller, but even with the flow rate of 1.3 L min⁻¹, the wall loses were still smaller

216 than 4 % and 2 % in the reaction chamber and the reference chambers, respectively, this indicates the

217 small effects of Ox loss to $P(O_3)_{net}$ measurements in our NPOPR detection system.

218 ***The transmittance of the light***. It is worth noting that there was still low transmittance of the light

219 ranged from 390 nm to 790 nm of the UV protection film, the reference chamber could not be regarded

220 as the totally dark condition, thus we tested the solar UV transmittance through the reaction and reference

221 chambers of the NPOPR detection system in the laboratory by using a sunlight simulation lamp (SERIC

222 XG-500B, Japan) to provide different intensities of illumination. The photolysis frequencies of the NO_2,

223 O_3, HONO, H_2O_2, NO₃_M (photolysis of NO_3 generates NO+O₂), NO₃_R (photolysis of NO_3 generates

224 NO₂+O), HCHO_M (photolysis of HCHO generates H₂+CO), and HCHO_R (photolysis of HCHO

225 generates H+HCO) inside and outside the reaction and reference chambers were measured using the

226 actinic flux spectrometer (PFS-100; Focused Photonics Inc, China). Table 1 presents the $J(NO_2)$, $J(O^1D)$,

227 and $J(HONO)$ results for outside and inside chambers, from this study and that from the literatures.

228 $J(H_2O_2)$, $J(NO_3\_M)$, $J(NO_3\_R)$, $J(HCHO\_M)$, and $J(HCHO\_R)$ are shown in Table S4. The photolysis

229 frequencies of all species inside the reaction chamber were in agree with those measured outside the

230 reaction chamber within 4 %. For the reference chamber, the transmittivity of $J(O^1D)$ and $J(NO_2)$ were

231   ~ 2 % and 9 %, respectively, the transmittivity of other species (i.e., $J(H_2O_2)$, $J(HCHO\_M)$ and

232    $J(HCHO\_R)$, etc.) were almost 0 %. Specifically, the transmittivity of $J(NO_3\_M)$ and $J(NO_3\_R)$ of

233   reference chamber were more than 90 % (Table S4). The influence of the different transmittivity of

234   different species will be discussed in Sect. 3. Table S4 shows the transmittivity of $J(H_2O_2)$, $J(NO_3\_M)$,

235    $J(NO_3\_R)$, $J(HCHO\_M)$, and $J(HCHO\_M)$ in the reaction chamber were more than 90 %. The

236   transmittivity of $J(H_2O_2)$, $J(HCHO\_M)$, and $J(HCHO\_M)$ of reference chamber were almost 0 %, but

237   the transmittivity of $J(NO_3\_M)$ and $J(NO_3\_R)$ of reference chamber were more than 90 %.

238

239   **Table 1. Photolysis frequency J (s^{-1}) of different species inside and outside the reaction and reference chambers.**

240   **The shaded and clear regions correspond to the photolysis frequencies with the reference (Ultem coated) and**

241   **reaction (clear) chambers, respectively. The transmittivity column shows the transmittivity of tested chambers**

242   **measurements with the set photolysis frequencies using SERIC XG-500B sunlight (this study) and ambient**

243   **(literatures).**

		Transmittivity		
	Averaged (this study)	Cazorla et al., 2010	Baier et al., 2015	Sadanaga et al., 2017
J_{NO2}	0.985 ±0.037	0.974	0.990	0.986
	0.094 ±0.014	0.021	0.01	0.121
J_{O3}	1.020 ±0.04	0.991	0.978	1.030
	0.019 ±0.011	0.0058	0.001	~0
J_{HONO}	0.983 ±0.037	0.976	0.982	0.988
	0.002 ±0.0002	0.0067	~0	0.017

244

245   ***The quantitative conversion efficiency of O_3 to NO_2 (α)*** in the NO-reaction chamber is crucial for

246   accurate measurement of $P(O_3)_{net}$. Here we used PFA tube (outer diameter of 12.7 mm; inner diameter

247   of 9.5 mm) as the NO-reaction chamber. The experimental schematic diagram is shown in Fig. S6. A

248   known concentration of O_3 was introduced into the NO-reaction chamber, NO reacts with O_3 and produce

249   NO_2, and the total NO_2 concentrations including that from the ambient air was measured using a CAPS-

250   NO_2 monitor ($[NO_2]_{CAPS}$). The O_3 concentration was controlled at approximately 310 ppbv according to

251   the maximum concentration range in the normal ambient atmosphere (to ensure that all ambient and

252   newly generated O_3 can react with NO and produce equivalent amount of NO_2). An O_3 generator

253   equipped with a low-pressure mercury lamp was employed to generate O_3, and the generated O_3

254   concentration ($[O_3]_g$) was measured by 2B O_3 monitor as mentioned above. Here we note that the O_3

255   concentration was diluted by the added NO/N$_2$ gas (with the flow rate of 20 mL min^{-1}) in the NO-reaction

256   chamber (with the total flow rate of 1.11 L min^{-1}), taking 1800 ppbv NO/N$_2$ gas as an example, the

257   relationship between [NO$_2$]$_{CAPS}$ and [O$_3$]$_g$ can be described by Eq. (3):

258    $$[NO_2]_{CAPS} = \frac{1.09}{1.11}[O_3]_g \alpha \qquad (3)$$

259   In order to determine the optimal length of the NO-reaction chamber and NO concentrations, we

260   did the cross test of α under the following scenarios: the NO-reaction chamber lengths were increased

261   from 30 to 650 cm in 50 cm step, and the NO standard gas (102.1 ppmv) was diluted to 600, 900, 1200,

262   1500, 1800, 2100, and 2400 ppbv in the NO-reaction chamber, the results are shown in Fig. 2. We found

263   that at [O$_3$]$_g$ was approximately 310 ppbv, with the NO concentrations ≥1800 ppbv in the NO-reaction

264   chamber, α could reach 99 %, 99.6 %, and 99.9 % with the NO-reaction chamber length of 50, 70, and

265   100 cm, respectively, where the corresponding O$_3$ residence time in NO-reaction chamber were 1.95 ,

266   2.74, and 3.91 s, respectively. Considering both the optimal reaction time in the NO-reaction chamber

267   and α, we selected the NO-reaction chamber length as 100 cm with the NO concentrations of 1800 ppbv

268   for the NPOPR detection system.
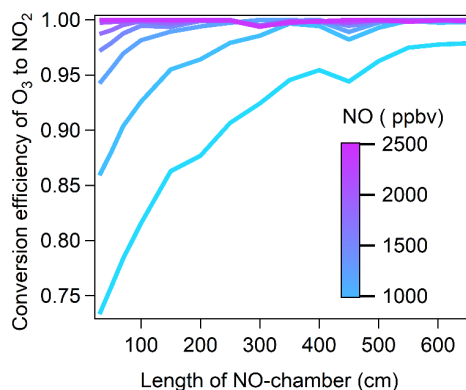
269

270   **Figure 2: The conversion efficiency of O$_3$ by NO to NO$_2$ in the NO-reaction chamber as a function of the NO-**

271   **chamber length, color coded with the NO concentrations.**

272   ***The airtightness of the reaction and reference chambers*** Here we also checked the airtightness

273   of the reaction and reference chambers by passing through gases with different flow rates, and compared

274   the values of [air flow rate × pressure] between the inlet and outlet of the chambers (as indicated in Fig.

275   3). We found that the deviation of [air flow rate × pressure] at the inlet and outlet of the reaction and

276   reference chambers at different flow rates were <3 % (as shown in Table S5), indicating the good

277   airtightness of the reaction and reference chambers. This will make sure that the photochemical reactions

278   in the reaction and reference chambers are not affected by the ambient air outside the chambers.
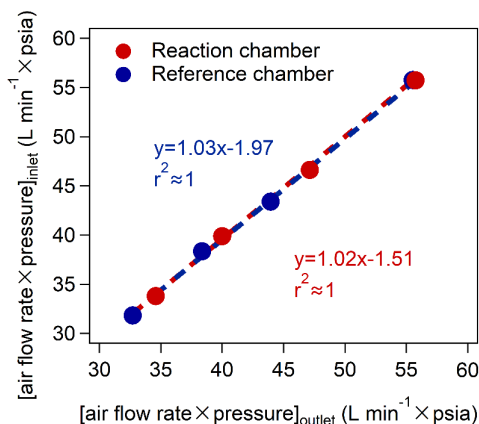
279

280   **Figure 3: The relationship of the values of [air flow rate × pressure] between the inlet and outlet of the**

281   **chambers (psia: Pounds Per Square Inch Absolute).**

282   ***The flow states in the reaction and reference chambers*** We calculated the Reynolds number to

283   check the gas flow state in the reaction and reference chambers. The Reynolds number (expressed as Eq.

284   (4)) is a dimensionless number that can be used as the basis for judging the flow characteristics of the

285   fluid:

286    $Re = \rho v d / \mu$ (4)

287   where v, ρ and μ are the flow velocity, density and viscosity coefficient of the fluid, respectively. In this

288   study, the fluid is air, d is the equivalent diameter of the reaction and reference chambers. The calculated

289   Reynolds number in the two chambers under the flow rates at 1.3, 2, 3, 4, and 5 L min^{-1} are 9.39, 14.58,

290   21.75, 29.05, and 36.34, respectively, indicating laminar flows in both chambers at different flow rates.

291   **2.3 Calibration and measurement error of CAPS-NO$_2$ monitor**

292   The Ox in NPOPR detection system was measured by the CAPS-NO$_2$ monitor. Detailed descriptions of

293   this technique can be found elsewhere (Kebabian et al., 2008, 2005). We calibrated the CAPS-NO$_2$

294   monitor as follows: a. injected ~ 10–100 ppbv of NO$_2$ for 30 minutes to passivate the surfaces of the

295   monitor and then injecting ultrapure air for ~ 10 minutes to ensure the zero point did not drift, according

296   to the ultrapure air condition, the LOD of CAPS was 0.88 and 0.02 ppbv (3 σ) at an integration time of

297   35 and 100 s, respectively; b. injected a wide range of NO$_2$ concentration (from 0–160 ppbv) prepared

298   from a NO_2 standard gas (with the original concentration of 2.08 ppmv) mixed with ultrapure air into the

299   CAPS-NO_2 monitor, repeated the experiments for three times at each NO_2 concentration, the final results

300   are shown in Fig. 4.

301   In order to get accurate measurement error of CAPS-NO_2 monitor ($(O_{X_{CAPS}})_{error}$), we fitted the

302   calibration results with a 68.3 % confidence level, and the blue line in Fig. 4 represents the maximum

303   fluctuation range under this confidence level, $(O_{X_{CAPS}})_{error}$ was then calculated from the fluctuation

304   range of the 68.3 % confidence interval of the calibration curve, the relationship between the

305    $(O_{X_{CAPS}})_{error}$ and the measured Ox value ($[Ox]_{measured}$) can be expressed as a power function curve, as

306   shown in Eq. (5) :

307    $$(O_{X_{CAPS}})_{error} = 9.72 \times [Ox]_{measured}^{-1.0024} \tag{5}$$

308   Subsequent $P(O_3)_{net}$ error estimation according to the instrument measurement error of CAPS-NO_2

309   monitor and the O_3 light-enhanced ingestion in the reaction and reference chambers are described in the

310   supplement (Sect. S2).
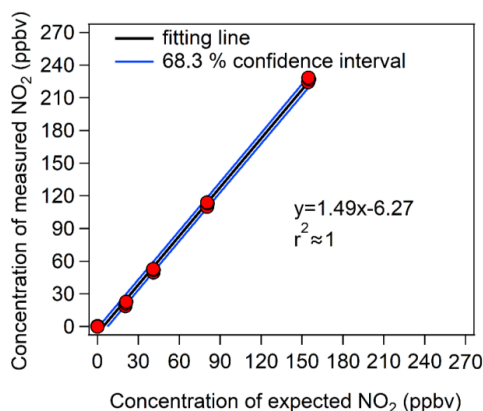
311

312   **Figure 4: Calibration results of CAPS-NO₂ monitor with different concentrations of NO₂, the y-axis**

313   **represented the NO₂ concentration measured by CAPS-NO₂ monitor, the x-axis represents the prepared NO₂**

314   **concentrations from the diluted NO₂ standard gas.**

315   **2.4 The LOD of the NPOPR detection system**

316   To test the LOD of the NPOPR detection system, the ultrapure air were introduced into the NPOPR

317   detection system in sequence to adjust the system for ~ 2 hours, followed by the ultrapure air or ambient

318   air when the time resolution of the CAPS NO_2 monitor was 1 s and the integration time period was 100

319   s (the measurement duration for the reaction and reference chambers are both 2 minutes), the LOD of the

320   NPOPR detection system was obtained at time resolutions of 4 minutes by propagating the errors of the

321   Ox measured by CAPS-NO$_2$ monitor when ultrapure air or ambient air was introduced into the NPOPR

322   detection system, combined with the related $\langle\tau\rangle$ under different flow rates, i.e., $\langle\tau\rangle$ was 0.063 h at the flow

323   rate of 5 L min^{-1}, the detailed calculation method is shown in Eq. (6):

324   $$LOD = \frac{3\times\sqrt{([Ox]_{rea\_STD})^2+([Ox]_{ref\_STD})^2}}{\tau} \tag{6}$$

325   where $[Ox]_{rea\_STD}$ and $[Ox]_{ref\_STD}$ represent the standard deviation of O$_X$ in the reaction and reference

326   chambers measured by CAPS-NO$_2$ monitor with the integration time period of 100 s, respectively. When

327   injecting ultrapure air, the LOD increases as the flow rate decreases, the LOD of the NPOPR detection

328   system was about 0.07, 1.4, and 2.3 ppbv h^{-1} at air flow rate of 1.3, 3, and 5 L min^{-1}, respectively, the

329   results are summarized in Table S6.

330   However, considering the background Ox concentration (measured by CAPS NO$_2$ monitor of the

331   air in the reference chamber) changes when measuring the ambient air, and the measured O$_X$ errors in

332   the reaction and reference chambers change with the Ox concentration (as shown in Sect. 2.3), the LOD

333   must also be a function of the intrinsic ambient and photochemically formed O$_3$ and NO$_2$ concentrations

334   (i.e. the Ox concentration measured by the CAPS NO$_2$ monitor). It's worth noting that the measured O$_X$

335   errors may be also influenced by the light-enhanced ingestion of O$_3$ in the reaction and reference

336   chambers under the ambient conditions when the light intensity (especially J_{O1D}) and O$_3$ concentration

337   are high, as tested and shown in the supplement (Sect. S2), but this effect is included in the measured O$_X$

338   errors. Therefore, when injecting the ambient air into the NPOPR system, the LOD can be calculated as

339   Eq. (7):

340   $$LOD = \frac{3\times\sqrt{(O_{X_\gamma})_{rea\_error}^2+((9.72\times[Ox]_{measured}^{-1.0024})_{ref\_error})^2+(O_{X_\gamma})_{ref\_error}^2+((9.72\times[Ox]_{measured}^{-1.0024})_{ref\_STD})^2}}{\tau} \tag{7}$$

341   where$(O_{X_\gamma})_{rea\_error}$ and $(O_{X_\gamma})_{ref\_error}$ represent the measurement error caused by the light-enhanced

342   ingestion of O$_3$ in the reaction and reference chambers, respectively; and $(9.72 \times$

343   $[Ox]_{measured}^{-1.0024})_{rea\_STD}$ and $(9.72 \times [Ox]_{measured}^{-1.0024})_{ref\_STD}$ represent the standard deviation

344   of O$_X$ in the reaction and reference chambers caused by CAPS-NO$_2$ monitor with the integration time

345   period of 100 s, respectively. More details about the $(O_{X_\gamma})_{rea\_error}$ and $(O_{X_\gamma})_{ref\_error}$ estimation method

346   can be found in the supplement (Sect. S2).

347   In conclusion, the LOD of the NPOPR detection system is determined by the measurement error of

348   Ox and the residence time. As the measurement error of the CAPS-NO_2 monitor decreases with the

349   increases of the Ox concentrations (as shown in Sect. 2.3), the higher limit values of the LOD could be

350   obtained when injecting the ultrapure air into the NPOPR detection system, which were approximately

351   0.07, 1.4, and 2.3 ppbv h^{-1} at air flow rate of 1.3, 3, and 5 L min^{-1}, respectively. During the field

352   observations, the LOD values are highly depend on the ambient conditions, especially the light intensity

353   and the Ox concentrations, higher O_3 concentrations and lower light intensity will likely resulted in lower

354   values of LOD.

355   **2.5 Laboratory tests of NPOPR detection system**

356   We conducted an experiment in the laboratory to test the performance of the NPOPR detection system at

357   Jinan University Panyu Campus (23.0° N, 113.4° E) on 26 March 2021. 5 L min^{-1} ambient air was

358   simultaneously injected into the reaction and reference chambers of the NPOPR detection system in

359   parallel, and the sunlight simulation lamp as mentioned above was used to simulate the sunlight radiation.

360   Light intensities of the sunlight simulation lamp were decreased from 26000 cd to 0 cd in step of 3700

361   cd. $P(O_3)_{net}$ was 28.6 ppbv h^{-1} at the light intensity of 26000 cd and gradually approaching 0 ppbv h^{-1} at

362   0 cd (as shown in Fig. 5), indicating that the $P(O_3)_{net}$ changing due to the different sunlight radiation

363   could be well captured by the NPOPR detection system.
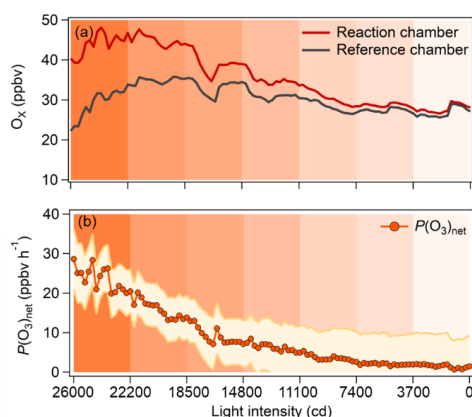
364

365   **Figure 5: (a) Measured Ox concentration in the reaction and reference chambers and (b) the related $P(O_3)_{net}$**

366   **as a function of the light intensity during the experiment.**

3 Atmospheric study and discussion

3.1 Field observation

The self-built NPOPR detection system was employed in the field campaign conducted at SZMGT, which is located in Shenzhen, China (as shown in the Supplement Sect. S3: Fig. S8), from 7 to 9 December 2021. During the campaign, in order to achieve the lowest O_3 and NO_2 wall loss, we used 5 L min^{-1} air flow rate in the reaction and reference chambers (with the residence time of ~ 4 minutes). Photolysis frequencies of different species were measured using the actinic flux spectrometer as mentioned above. O_3 and NO_X ($NO+NO_2$) concentrations were measured using a 2B O_3 monitor and a chemiluminescence NOx monitor (Model 42i, Thermo Fisher Scientific, USA), respectively. T and RH were measured by a portable weather station (Met Pak, Gill Instruments Ltd, UK). The VOCs were measured by a high-resolution proton transfer reaction time-of-flight mass spectrometry (PTR-ToF-MS, Ionicon Analytik, Austria) (Wang et al., 2020a; Wu et al., 2020) and an off-line GC-MS-FID technique (Wuhan Tianhong, Co. Ltd, China) (Yuan et al., 2012) (Table S8). Additionally, a self-built formaldehyde analyzer was used to detect formaldehyde (HCHO) (Zhu et al., 2020). Figure 6 presents the temporal and diurnal variations of $P(O_3)_{net}$, O_X, O_3, NO, NO_2, NO_X, T, RH, $J(O^1D)$, and $J(NO_2)$ concentrations at SZMGT during the campaign.

383
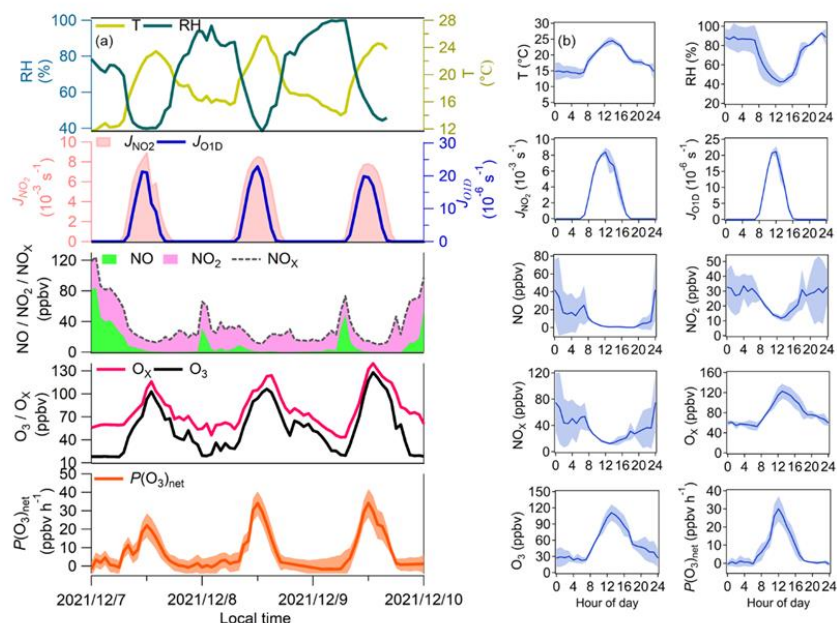
Figure 6: (a) Time series and (b) diurnal of $P(O_3)_{net}$, $J(NO_2)$, $J(O^1D)$, T, RH, O_X, NO_2 and NO measured at
SZMGT from 7 to 9 December 2021. The shaded areas represent the error of each measured species, where
the error of $P(O_3)_{net}$ was calculated according to the method described in the supplement (Sect. S2) (the
estimation of the $P(O_3)_{net}$ error).

During the measurement period, the $P(O_3)_{net}$ ranged from ~ 0 to 34.1±7.8 ppbv h^{-1}, with the daytime

(from 6:00–18:00) average value of 12.8 (±5.5) ppbv h^{-1}, the maximum $P(O_3)_{net}$ at SZMGT was lower

than that measured at the urban area of Houston in US (40–50 ppbv h^{-1} and 100 ppbv h^{-1} in autumntime

and springtime, separately) (Baier et al., 2015; Ren et al., 2013), close to that measured at the Indiana in

US (~ 30 ppbv h^{-1} in springtime) (Sklaveniti et al., 2018), and much higher than that measured at the

Wakayama Forest Research Station, a remote areas of Japan (10.5 ppbv h^{-1} in summertime) (Sadanaga

et al., 2017) and the urban area of Pennsylvania in US (~ 8 ppbv h^{-1} in summertime) (Cazorla et al., 2010).

The result indicates the rationality of the measured $P(O_3)_{net}$ in this study. From previous studies, the O_3

pollution in the PRD area was more severe in summer and autumn than in winter and spring (Zhang et

al., 2021). In this study, the $P(O_3)_{net}$ was measured in wintertime, which was already high, so we believe

that the O_3 pollution of PRD is severe and urgently needs to be controlled. More measurements of $P(O_3)_{net}$

worldwide are listed in Table S7, we found that $P(O_3)_{net}$ is much higher in urban areas than that in remote

areas using both modelling or direct measurement methods.

401   According to the diurnal variation of all the measured pollutants indicators, $P(O_3)_{net}$ started to

402   increase at around 7:00 am at local time, this may be due to two reasons: (1) the rise of the O_3 precursors

403   (i.e., VOCs) due to high-altitude atmospheric residual layer transported down to the near-surface at this

404   time; (2) the increase of solar radiation intensity after 7:00 am, which increased the oxidation capacity

405   of the pollutants. These two factors jointly enhanced the photochemical oxidation reaction of VOCs and

406   gradually increased $P(O_3)_{net}$. $P(O_3)_{net}$ was then reached a peak at around 12:00 at noon time, which was

407   consistent with $J(NO_2)$, but this peak time was earlier than that of O_3, which peaks at around 14:00, this

408   may be due to the photochemical reactions dominate O_3 concentration changes between 12:00 and 14:00.

409   After 14:00, the O_3 concentration started to decrease, this may be due to other processes dominated O_3

410   concentration changes at this time, such as O_3 reacted with other pollutants, or the surface deposition and

411   the outflow of O_3 by physical transport. In conclusion, changes of O_3 concentrations were influenced by

412   both photochemical production and physical transport.

413   **3.2 Model simulation of $P(O_3)net$ in the reaction and reference chambers**

414   Based on the field observation data, we modeled the ozone production rate $P(O_3)$ and ozone destruction

415   rate $D(O_3)$ during the 4-minute photochemical reaction in the reaction and reference chambers at 12:00

416   on 7 December 2021, using a zero-dimensional box model based on the Framework for 0-D Atmospheric

417   Modeling (F0AM) v3.2 (Wolfe et al., 2016) coupled with MCM v3.3.1, which contains a total of 143

418   VOCs, more than 6700 species, involving more than 17000 reactions (Jenkin et al., 2015). $P(O_3)_{net}$ can

419   be expressed by the difference between $P(O_3)$ and $D(O_3)$, $P(O_3)$ and $D(O_3)$ can be expressed as Eq. (8)–

420   (9).

421     $$P(O_3) = k_{HO_2+NO}[HO_2][NO] + \sum_i k_{RO_{2,i}+NO}[RO_{2i}][NO]\varphi_i \tag{8}$$

422     $$D(O_3) = k_{O(^1D)+H_2O}[O(^1D)][H_2O] + k_{OH+O_3}[OH][O_3] + k_{HO_2+O_3}[HO_2][O_3]$$

423     $$+ \sum_i \left(k_{O_3+Alkene_i}[O_3][Alkene_i]\right) + k_{OH+NO_2}[OH][NO_2] + k_{RO_2+NO_2}[RO_2][NO_2] \tag{9}$$

424   where k_{M+N} represents the bimolecular reaction rate constant of M and N, and φ_i is the yield of NO_2 from

425   the reaction RO_{2i} +NO. The relevant reaction rates of $P(O_3)$ and $D(O_3)$ and the VOCs concentrations

426   during 7–9 December 2021 in SZMGT used in the model are listed in Tables 2 and S8.

427   **Table 2. O_3 production and destruction reactions and the relevant reaction rates used in the model.**

Reactions	Rate coefficient / unit	Number

O₃ production pathways - $P(O_3)$		
$RO_2 + NO \rightarrow RO + NO_2$	$2.7\times10^{-12}\times exp(360/T)$ / molecules^{-1} cm^3 s^{-1}	(R1)
$HO_2 + NO \rightarrow OH + NO_2$	$3.45\times10^{-12}\times exp(270/T)$ / molecules^{-1} cm^3 s^{-1}	(R2)
O₃ loss pathways - $D(O_3)$		
$O_3 + hv \rightarrow O^1D + O_2$	Measured JO^1D / s^{-1}	(R3)
$O_3 + C_2H_4 \rightarrow HCHO + CH_2OOA$	$9.1\times10^{-15}\times exp(-2580/T)$ / molecules^{-1} cm^3 s^{-1}	(R4)
$O_3 + C_3H_6 \rightarrow CH_2OOB + CH_3CHO$	$2.75\times10^{-15}\times exp(-1880/T)$ / molecules^{-1} cm^3 s^{-1}	(R5)
$O_3 + C_3H_6 \rightarrow CH_3CHOOA + HCHO$	$2.75\times10^{-15}\times exp(-1880/T)$ / molecules^{-1} cm^3 s^{-1}	(R6)
$O_3 + C_5H_8 \rightarrow CH_2OOE + MACR$	$3.09\times10^{-15}\times exp(-1995/T)$ / molecules^{-1} cm^3 s^{-1}	(R7)
$O_3 + C_5H_8 \rightarrow CH_2OOE + MVK$	$2.06\times10^{-15}\times exp(-1995/T)$ / molecules^{-1} cm^3 s^{-1}	(R8)
$O_3 + C_5H_8 \rightarrow HCHO + MACROOA$	$3.09\times10^{-15}\times exp(-1995/T)$ / molecules^{-1} cm^3 s^{-1}	(R9)
$O_3 + C5H_8 \rightarrow HCHO + MVKOOA$	$2.06\times10^{-15}\times exp(-1995/T)$ / molecules^{-1} cm^3 s^{-1}	(R10)
$O_3 + HO_2 \rightarrow OH$	$2.03\times10^{-16}\times (T/300)^{4.57}\times exp(693/T)$ / molecules^{-1} cm^3 s^{-1}	(R11)
$RO_2 + NO_2 \rightarrow$ peroxy nitrates	$(3.28\times10^{-28}\times7.24\times10^{18}\times P/T\times(T/300)^{-6.87}\times1.125$ $\times10^{-11}\times(T/300)^{-1.105})\times10^{(log10(0.30)}/(1+(log10(2.93$ $\times10^{-17}\times7.24\times10^{18}\times P/T\times(T/300)^{-5.765})/0.75-1.27$ $\times log10(0.30))^2))/(2.926\times10^{-17}\times7.24\times10^{18}\times P/T$ $\times(T/300)^{-5.765})$ / molecules^{-1} cm^3 s^{-1}	(R12)
$NO_2 + OH \rightarrow HNO_3$	$3.2\times10^{-30}\times7.24\times10^{18}\times P/T\times(T/300)^{-4.5}\times3\times10^{-11}$ $\times10^{log10(0.41)}/(1+(log10(3.2\times10^{-30}\times7.24\times10^{18}\times P/T$ $\times(T/300)^{-4.5}/3\times10^{-11})/(0.75-1.27$ $\times(log10(0.41))^2)/(3.2\times10^{-30}\times7.24\times10^{18}\times P/T$ $\times(T/300)^{-4.5}+3\times10^{-11})$ / molecules^{-1} cm^3 s^{-1}	(R13)
$O_3 + OH \rightarrow HO_2$	$1.70\times10^{-12}\times exp(-940/T)$ / molecules^{-1} cm^3 s^{-1}	(R14)

428   *The rate coefficient obtained from the MCM v3.3.1 model.

429   In total three stages simulations were carried out to obtain the 4-minute photochemical reactions

430   in the reaction and reference chambers, all these three stages model were operated in a time-dependent

431   mode with a 1 s resolution. In the 1st stage, in order to establish a real atmospheric environment system,

432   all the observation items on 7 November 2021, 6:00-11:30 was used to constrain the model to obtain the

433   concentration of the unmeasured species in the genuine atmosphere. Including oxygenated volatile

434   organic compounds (in total 16 species), non-methane hydrocarbons (in total 47 species), O₃, NO, NO₂,

435   J value, T, RH, and pressure (P). Since O₃-NO-NO₂ was not in a steady state when all species were

436   constrained, we conducted a 2nd stage simulation during 11:30–12:00. In this stage, we used the output

437   concentration of the unmeasured species from the simulation in the last 1 s of the 1st stage simulation as

438   the input, which were not constrained after giving initial values. For the measured species, O₃, NO, and

439   NO_2 were no longer constrained after giving initial values, while all other items (including NO_X, VOCs,

440   J value, RH, T, P, etc.) were still constrained in a time-dependent mode with a 1 s resolution after giving

441   initial values. In the 3rd stage, we modelled the 4-minute photochemical reactions in the reaction and

442   reference chambers. We used the output concentration of the unmeasured species (i.e., OH, HO_2, RO_2,

443   SO_2, HONO, etc.) from the simulation in the last 1 s of the 2nd stage simulation and all the measured item

444   (i.e., O_3, NO, NO_2, VOCs, J value, RH, T, P, etc.) as the model input, which were not constrained after

445   giving initial values. Figure 7 is an explicit explanation of the 3rd stage simulation.
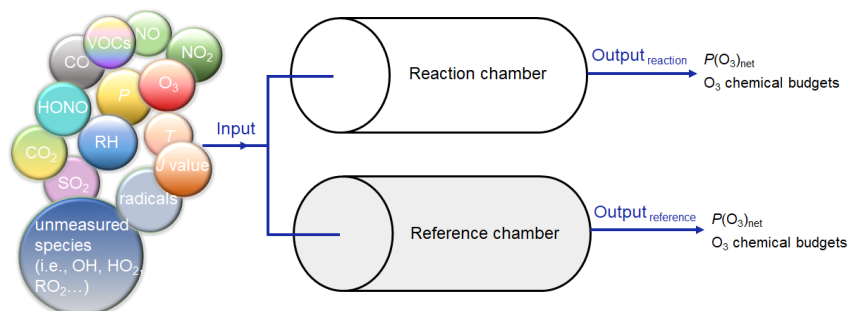
446

447   **Figure 7: Explicit explanation of the 3rd stage model simulation (input meteorological conditions: P: 1015.3**

448   **hPa, T: 295.6 K, RH: 39.7 %).**

449

450   Specifically, as the photolysis frequencies play critical roles in the simulation of $P(O_3)_{net}$, the J

451   values obtained from two methods (labeled as method I and method II) were used in the 3rd stage 4-

452   minute simulation. J values used in method I were obtained from the measured values (including $J(NO_2)$,

453    $J(O^1D)$, $J(HONO)$, $J(H_2O_2)$, $J(NO_3\_M)$, $J(NO_3\_R)$, $J(HCHO\_M)$, and $J(HCHO\_R)$) and the simulated values

454   using the Tropospheric Ultraviolet and Visible (TUV) radiation model (version 5.3) (including $J(HNO_3)$,

455    $J(CH_3CHO)$, $J(MACR)$, $J(MEK)$, $J(HOCH_2CHO)$, $J(C_2H_5CHO)$, $J(C_3H_7CHO)$, and $J(C_4H_9CHO)$, etc.), while J

456   values in method II were all obtained from the simulated values using TUV model, detailed information

457   of these two methods are introduced in the Supplement (Sect. S4) (Tables S9 and S10). The variation of

458   the radicals (i.e., HO_2, OH, RO_2, and NO_3) and NO, NO_2, and O_3 concentrations obtained from method

459   I and method II during the 3rd stage 4-minute model simulation are shown in Fig. 8 and Fig. S9,

460   respectively. The production and destruction reactions of RO_X (=$OH+HO_2+RO_2$) in the reaction and

461   reference chambers obtained from method I and II are shown in Fig. 9 and Fig. S10, respectively, and

462   the final modeling results are put in Fig. 10 and Fig. S11, respectively.

463   From Fig. 8, in the reaction chamber, HO_2, OH, RO_2, and NO_3 concentrations first slightly

464 increased and then became stable, their final concentrations were 2.00×10^8, 7.64×10^6, 1.08×10^8, and

465 8.47×10^6 molecules cm^{-3}, respectively. In the reference chamber, HO$_2$ and RO$_2$ concentrations dropped

466 during the 1st half minute and roses afterwards, the final HO$_2$ concentration (1.35×10^8 molecules cm^{-3})

467 was lower than that in the reaction chamber, while the RO$_2$ concentration exceed that in the reaction

468 chamber at the end of the 2nd minute and gradually became stable at 1.27×10^8 molecules cm^{-3}; the OH

469 concentration dropped significantly at the 1st minute and then became stable at around 6.16×10^5

470 molecules cm^{-3}; the NO$_3$ concentration rose significantly during the 4-minute simulation and became

471 3.55×10^7 molecules cm^{-3} at the end, which was much higher than that in the reaction chamber. The

472 decrease of HO$_2$ and RO$_2$ concentrations in the 1st half minute in the reference chambers may be due to

473 the NO titration effects, as high NO concentration existed at the 1st half minute, the increase of HO$_2$ and

474 RO$_2$ concentrations afterwards were largely attributable to the VOCs+NO$_3$ oxidation reaction, and

475 partially due to the decomposition of PANs and HO$_2$NO$_2$, as well as the OVOC photolysis (see Fig. 9b),

476 all of above mentioned reactions could contribute to the HO$_2$ and RO$_2$ concentration increase. The NO$_3$

477 sources in the reference chamber including the NO$_2$+O$_3$ reaction and the N$_2$O$_5$ decomposition, the NO$_3$

478 consumption including its reaction with VOCs and NO, therefore, the NO$_3$ concentration increase in the

479 reference was jointly influenced by NO, NO$_2$, O$_3$, and VOCs. However, the effects of the increase of NO$_2$

480 concentration in the reference chamber will be neutralized by the decrease of O$_3$ concentration, therefore,

481 the much higher NO$_3$ concentration in the reference chamber compared to that in the reaction chamber

482 may be mainly due to the much less consumption of NO$_3$ by NO$_3$+NO reaction, more details about the

483 production and destruction rates of ROx are shown in Fig. 9.
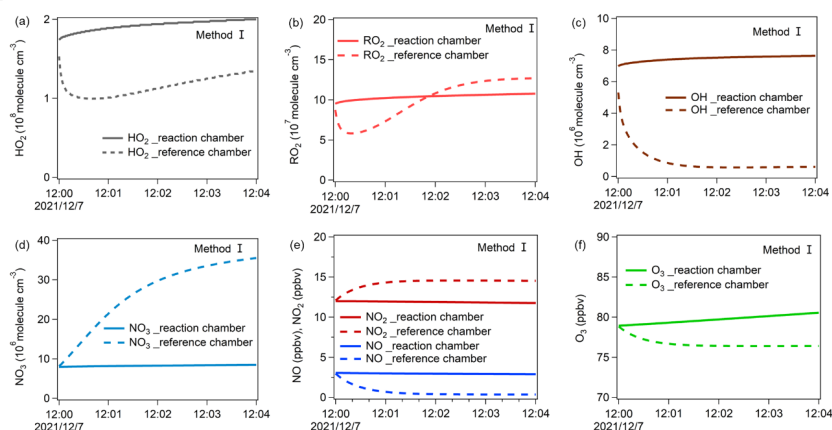
484

485   **Figure 8: The variations of (a)HO_2, (b) RO_2, (c) OH, (d)NO_3, (e) NO, NO_2, and (f) O_3 concentrations during**

486   **the 3rd stage 4-minute model simulation using method I. The concentration changes of these items using**

487   **method II is shown in Fig. S9.**

488
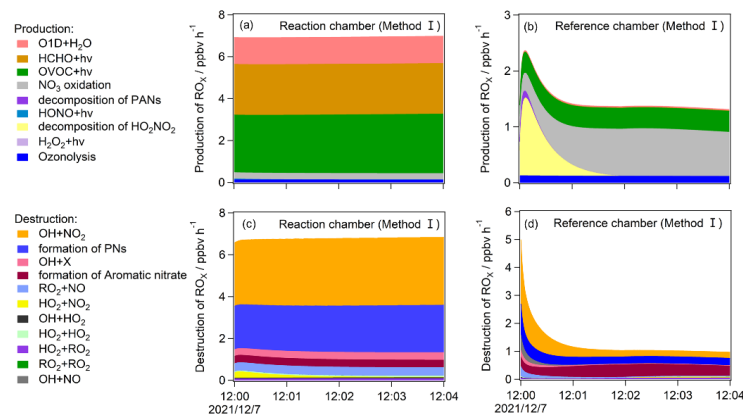
489   **Figure 9: The production and destruction pathways of RO_X during the 3rd stage 4-minute model simulation**

490   **in the reaction and reference chambers. (PAN: Peroxyacetyl Nitrate; PNs: formations of all peroxynitrate**

491   **(including $CH_3O_2NO_2$ and PAN; X: PAN and the net loss of OH+NO to form HONO (usually small)). The**

492   **production and destruction pathways of these items using method II is shown in Fig. S10.**

493   Figures 10a–d show the modeled $P(O_3)_{net}$ and the source and sink of various species during the 3rd

494   stage 4-minute simulation. Figure 10a shows the steady state of $P(O_3)_{net}$ and the various species in the

495   ambient atmosphere achieved in the last 1 s of the 2nd stage simulation; Figures 10b and c show the

496   modeled $P(O_3)_{net}$ and the O_3 chemical budgets in the reaction and reference chambers during the model

497   simulation period; Figure 10d summarized the modeled $P(O_3)_{net}$ in the ambient atmosphere, and that in

498   the reaction and reference chambers, in order to compare the modeled results with our measurement

499   results, we calculated the integral mean of the modeled $P(O_3)_{net}$ in the reaction and reference chambers

500   and appended the related measured $P(O_3)_{net}$ value during this 4-minute simulation time onto Fig. 10d.

501   Further, the reaction weights of different production and destruction reactions process of O_3 are shown

502   in Figs. 10e–h.
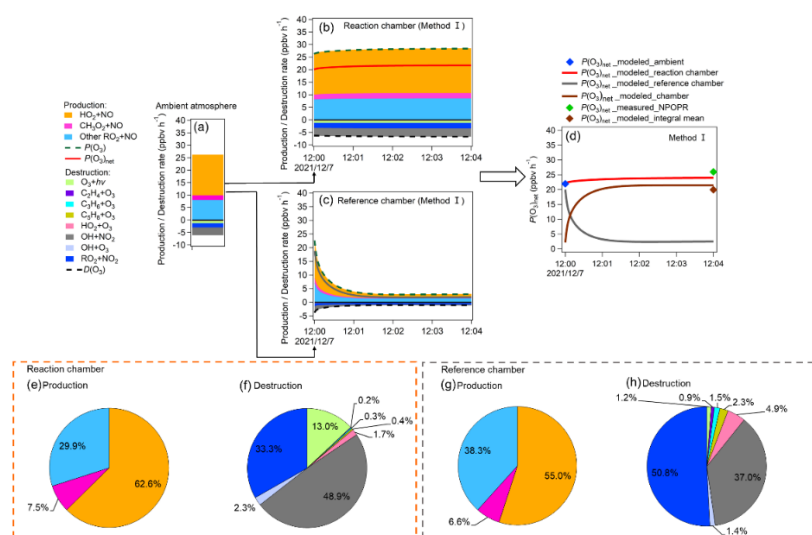
Figure 10: (a)–(c) show the modeled $P(O_3)_{net}$ and the O_3 chemical budgets in (a) the ambient atmosphere when inject into the reaction and reference chambers, (b–c) the reaction and reference chambers during the 4-minute model simulation, (d) shows variable $P(O_3)_{net}$, where $P(O_3)_{net}$_modeled_ambient represent the modeled $P(O_3)_{net}$ from the last 1 s of the 2nd stage simulation, $P(O_3)_{net}$_modeled_reaction chamber and $P(O_3)_{net}$_modeled_reference chamber represent the $P(O_3)_{net}$ changing trend during the 4-minute photochemical reactions in the reaction and reference chambers, respectively, $P(O_3)_{net}$_modeled_chamber= $P(O_3)_{net}$_modeled_reaction chamber–$P(O_3)_{net}$_modeled_reference chamber, $P(O_3)_{net}$_modeled_integral mean represent the integral mean of the $P(O_3)_{net}$_modeled_chamber, and $P(O_3)_{net}$_measured_NPOPR represent the measured $P(O_3)_{net}$ by NPOPR detection system. (e)–(h) show the reaction weights of each production and destruction reactions process of O_3 in the reaction and reference chambers in method I.

Figure 10a-h show the contribution of different reaction pathways to $P(O_3)$ and $D(O_3)$. The $P(O_3)$ and $D(O_3)$ were almost the same within the 4-minute reaction in the reaction chamber (all species reached a steady state condition), while the $P(O_3)$ and $D(O_3)$ in the reference chamber decreased significantly within the 1st minute, and kept stable in the following minutes. In the reaction chamber, the HO$_2$+NO reaction contributed most to $P(O_3)$, accounting for 62.6 % of the total $P(O_3)$, with the integral mean value of 17.5 ppbv h^{-1} in the reaction chamber. The second important pathway of $P(O_3)$ was RO$_2$+NO (occupied 37.4 % of the total $P(O_3)$). The reaction of RO$_2$+NO contained more than around 1200 types of RO$_2$ radicals, and the pathway of CH$_3$O$_2$+NO contributed 7.5 % of the total $P(O_3)$. The most important contributor of $D(O_3)$ was OH+NO$_2$ (48.9 %), followed by RO$_2$+NO$_2$ (33.3 %), O$_3$ photolysis (13.0 %), O$_3$+OH (2.3 %), O$_3$+HO$_2$ (1.7 %), C$_5$H$_8$+O$_3$ (0.4 %), C$_3$H$_6$+O$_3$ (0.3 %), and C$_2$H$_4$+O$_3$ (0.2 %). In the reference chamber, the integral mean value of HO$_2$+NO reaction was 2.3 ppbv h^{-1}, which had the largest

526 contribution to $P(O_3)$ (accounting for 55.0 %). The second largest contributor of $P(O_3)$ was RO_2+NO

527 (occupied 44.9 % of the total $P(O_3)$), in which the pathway of CH_3O_2+NO contributed 6.6 % of the total

528 $P(O_3)$. The most important contributor of $D(O_3)$ was RO_2+NO_2 (50.8 %), followed by OH+NO_2 (37.0 %),

529 O_3+HO_2 (4.9 %), C_5H_8+O_3 (2.3 %), C_3H_6+O_3 (1.5 %), O_3+OH (1.4 %), O_3 photolysis (1.2 %), and

530 C_2H_4+O_3 (0.9 %). For all $P(O_3)$ reactions, the weight of RO_2+NO reaction in the reference chamber was

531 7.5 % higher than that in the reaction chamber, however, for all $D(O_3)$ reactions, the weight of RO_2+NO_2

532 reaction in the reference chamber was 17.5 % higher than that in the reaction chamber, which will

533 somehow mitigate the high $P(O_3)$ caused by RO_2+NO in the reference chamber. Further, the weight of

534 OH+NO_2 reaction in the reference chamber was 11.9 % lower than that in the reaction chamber, which

535 may be the main reason that led to NO_2 concentration in the reference chamber was much higher than

536 that in the reaction chamber. It is worth noting that the different reaction pathways of $P(O_3)$ and $D(O_3)$

537 had stabilized at around 1.5 minute for both method I and II (as shown in Figs. 10 and S11), and the

538 radicals that play critical roles in photochemical O_3 formation, such as HO_2, RO_2 and OH, reached

539 quasi-steady states in about 3 minutes (as shown in Figs. 8 and S9). As the lowest experimental

540 residence time in the reaction and reference chambers was 3.8 min at the air flow rate of 5 L min^{-1}, the

541 photochemical reaction time at different air flow rates in the NPOPR system is sufficient enough

542 for investigating the $P(O_3)_{net}$, and it is reasonable for us to set the alternate ambient air sampling time

543 for the reaction and reference chambers at 2 minutes, where the ambient air actually has already reacted

544 for at least 3.8 minutes in the chambers.

545 The $P(O_3)_{net}$ measured by the NPOPR detection system at 12:04 was 26.0 ppbv h^{-1}, which was 7.5

546 ppbv h^{-1} higher than the modeled $P(O_3)_{net}$ value (18.5 ppbv h^{-1}, calculated from the integral mean of the

547 3rd stage 4-minute modeled $P(O_3)_{net}$ in Fig. 10d). Here we would like to note that, in order for a better

548 comparison between the measured and modeled $P(O_3)_{net}$ values, the measured $P(O_3)_{net}$ used here was

549 obtained from 4-minute time resolution, which is 1.4 ppbv h^{-1} higher than the measured $P(O_3)_{net}$ value

550 used in Fig. 6 (1-hour time resolution). The ratio of measured and modeled $P(O_3)_{net}$ values is 1.4, which

551 is consistent with the measured-to-modeled ratio of the cumulative $P(O_3)_{net}$ (1.3 and 1.4) obtained from

552 previous studies (Cazorla et al., 2012; Ren et al., 2013), where $P(O_3)_{net}$ values were also measured

553 directly in the atmosphere and were independent of the OH and HO_2 measurements. The reason for the

554 difference between measured and modeled $P(O_3)_{net}$ here may be due to the inaccurate estimation of

555   HO$_2$/RO$_2$ radicals, for example, Ren et al. (2013) found that the $P(O_3)$ calculated from the modeled HO$_2$

556   was lower than that calculated from the measured HO$_2$. The unknown HO$_2$ source should be identified

557   for a more accurate estimation of $P(O_3)_{net}$ in future study.

558   Additionally, the modeled $P(O_3)_{net}$ using the J values obtained from method II was 9.3 ppbv h^{-1}

559   lower than the measured $P(O_3)_{net}$, this discrepancy was slightly larger than that using method I, as shown

560   in the supplement (Sect. S4) (Fig. S11), the differences of the measured and modeled $P(O_3)_{net}$ by method

561   I and method II were 28.8 % and 35.8 %, respectively, this difference was mainly due to the transmittance

562   of $J(NO_2)$ in method II (30 %) was much higher than that in method I (9 %), NO$_2$ photolysis products

563   NO, it involved in the main reaction of O$_3$ production of HO$_2$+NO and RO$_2$+NO, so the modeled $P(O_3)_{net}$

564   in the reference chamber was slightly overestimated in method II, thus leading to an underestimation of

565   final $P(O_3)_{net}$.

566   In conclusion, modeling tests demonstrated that the radicals and gas species in the reaction

567   chamber of NPOPR detection system were similar to that in the genuine ambient air, while these radicals

568   were also present unexpectedly existed in the reference chamber. This was mainly due to the UV

569   protection film used by the reference chamber does not completely filtered out the sunlight, which led to

570   the low transmittance of the light ranged from 390 nm to 790 nm. The bias of the $P(O_3)_{net}$ caused by this

571   interference modeled in method I and method II were 13.9 % and 22.3 %, respectively, this make us

572   ensure that the measured $P(O_3)_{net}$ by NPOPR detection system should be regarded as the lower limit

573   values of real $P(O_3)_{net}$ in the atmosphere. We recommend the J values obtained from method I should be

574   used in the model simulation, which can better explain the photochemical formation of O$_3$ in the actual

575   atmosphere, but if the direct J value measurement cannot be achieved during the field observation

576   campaign, the J values obtained from method II was also acceptable in modeling study.

577

578   **4 Conclusions**

579   We modified and improved a net photochemical ozone production rate (NPOPR) detection system based

580   on a dual-channel reaction chamber technique, which can work more accurately and widely used

581   compared to previous studies. The main improvements of NPOPR detection system compared to

582   previous studies were as follows: (1) improved the design of the reaction and reference chambers to make

583   sure they have good airtightness; (2) changed the air sampling structure to enable the total air flow rates

584   change freely from 1.3 to 5 L min^{-1} in the reaction and reference chambers, which can make the NPOPR

585   system achieve different LOD and appliable to different ambient environment; (3) characterized the

586   NPOPR detection system at different air flow rates to optimize the $P(O_3)_{net}$ measurements, the limit of

587   detection (LOD) of the NPOPR detection system are 0.07, 1.4, and 2.3 ppbv h^{-1} at air flow rates of 1.3,

588   3, and 5 L min^{-1}, respectively; (4) tested the performance of both reaction and reference chambers by

589   combining the field measurement and the MCM modelling method.

590   The NPOPR detection system was employed in the field observation at the Shenzhen

591   Meteorological Gradient Tower (SZMGT), which is located in PRD, China. During the measurement

592   period, the $P(O_3)_{net}$ was around zero during nighttime and ranged from ~ 0 to 34.1±7.8 ppbv h^{-1} during

593   daytime (from 6:00–18:00), with the average value of 12.8 (±5.5) ppbv h^{-1}. Besides, $P(O_3)_{net}$ start to

594   increase at around 7:00 am at local time, this may be due to the rise of the O_3 precursors (i.e., VOCs)

595   transported down from the high-altitude atmospheric residual layer to the near-surface and the increase

596   of solar radiation intensity increased the atmospheric oxidation capacity. $P(O_3)_{net}$ was then reaches a peak

597   at around 12:00 at noon time, by coupling with diurnal O_3 concentration trends, we confirmed that the

598   ground-level O_3 concentrations were influenced by both photochemical production and physical

599   transport.

600   In order to clarify the detailed photochemical reaction processes in the reaction and reference

601   chambers of NPOPR system, we modeled the $P(O_3)_{net}$ on 7 December 2021, 12:00-12:04 in the reaction

602   and reference chambers using MCM v3.3.1. As the photolysis frequencies of different species (J values)

603   play critical roles in the formation of $P(O_3)_{net}$, the J values obtained from two methods were used in the

604   4-minute chamber photochemical reaction (labeled as method I and method II), in method I , eight main

605   J values (e.g., $J(NO_2)$, $J(O^1D)$, $J(HONO)$, etc.) were measured directly, and other J values were obtained

606   from the simulated values using the Tropospheric Ultraviolet and Visible (TUV) radiation model, while

607   in method II, J values were all obtained from the simulated values using TUV model (as described in

608   Sect. 3.2). Modeling tests demonstrated that the concentration of different radicals and gas species (i.e.,

609   OH, HO_2, RO_2, NO_3, NO, NO_2, and O_3) in the reaction chamber were similar with those in the real

610   ambient environment, while due to the UV protection film used by the reference chamber does not

611   completely filtered out the sunlight, there was low transmittance of the light ranged from 390 nm to 790

612   nm. In the reaction chamber, the contribution of different reactions to $P(O_3)$ and $D(O_3)$ modeled by

613   method I and II were quite similar, where the HO_2+NO reaction contributed most to $P(O_3)$ (~ 62.6 %),

614   followed by the RO_2+NO reaction (~ 37.4 %). The $OH+NO_2$ reaction contributed most to $D(O_3)$, which

615   accounted for ~ 48.9 %, followed by the RO_2+NO_2 reaction O_3 photolysis, which accounted for ~ 33.3 %

616   and 13.0 %, respectively. In the reference chamber, the contribution of different reactions to $P(O_3)$ and

617    $D(O_3)$ modeled by method I and II were different, where the HO_2+NO reaction contributed ~ 55.0 % and

618   ~ 58.2 % to the total $P(O_3)$, respectively, and RO_2+NO contributed ~ 44.9 % and 41.8 % to the total

619    $P(O_3)$, respectively. The most important contributor of $D(O_3)$ modeled by method I was RO_2+NO_2

620   (50.8 %), followed by $OH+NO_2$ (37.0 %), while the most important contributor of $D(O_3)$ modeled by

621   method II was $OH+NO_2$ (46.8 %), followed by RO_2+NO_2 (44.1 %). For all $P(O_3)$ reactions, the weight

622   of RO_2+NO reaction in the reference chamber was 7.5 % and 4.3 % higher than that in the reaction

623   chamber in method I and II, respectively, however, for all $D(O_3)$ reactions, the weight of RO_2+NO_2

624   reaction in the reference chamber was 17.5 % and 10.9 % higher than that in the reaction chamber in

625   method I and II, respectively, which will somehow mitigate the high $P(O_3)$ caused by RO_2+NO in the

626   reference chamber. The different reaction pathways of $P(O_3)$ and $D(O_3)$ had stabilized at around 1.5

627   minute, and the radicals that play critical roles in photochemical O_3 formation, such as HO_2, RO_2

628   and OH, reached quasi-steady states in about 3 minutes, the long enough ambient air residence time

629   in the reaction and reference chambers ($\geq$ 3.8 min) make the photochemical reaction time at different

630   air flow rates in the NPOPR system sufficient enough for investigating the $P(O_3)_{net}$, and it is

631   reasonable for us to set the alternate ambient air sampling time for the reaction and reference chambers

632   at 2 minutes, where the ambient air actually has already reacted for at least 3.8 minutes in the chambers.

633   The bias of the modeled $P(O_3)_{net}$ caused by the interference of the reactions in the reference

634   chamber in method I and method II were 13.9 % and 22.3 %, respectively, thus the measured $P(O_3)_{net}$ by

635   NPOPR detection system should be regarded as the lower limit values of real $P(O_3)_{net}$ in the atmosphere.

636   Still, the measured $P(O_3)_{net}$ were 7.5 and 9.3 ppbv h^{-1} higher than the modeled $P(O_3)_{net}$ obtained from

637   method I and II, respectively, which may be due to the inaccurate modelling of HO_2/RO_2 radicals. Short-

638   lived intermediates measurements coupling with direct $P(O_3)_{net}$ measurements are needed in future study

639   in order to understand the photochemical production and destruction mechanisms of O_3 better. We

640   recommend the J values obtained from method I should be used in the model simulation, which can

641   better explain the photochemical formation of O_3 in the actual atmospheric environment, but if the direct

642   J value measurement cannot be achieved during the observation campaign, the J values obtained from

643   method II was also acceptable in modeling study.

644   The self-built NPOPR detection system in this study filled the blank of the observation method in

645   China. The research results not only help us to understand tropospheric O_3 budget, but also provide an

646   important data basis for formulating correct O_3 pollution prevention measures and control strategies.

647

648   *Data availability.* The observational data used in this study are available from corresponding authors

649   upon request (junzhou@jnu.edu.cn).

650   *Author contributions.* JZ, BY, and MS designed the experiment, YXH and JZ developed and assembled

651   the NPOPR detection system, YXH, JZ, JPZ, BY, YW, YFW, SCY, YWP, JPQ, XJH, XS and YBC

652   collected and analyzed the data. YXH and JZ wrote the manuscript, all authors revised the manuscript.

653   *Competing interests.* The authors declare that they have no known competing interests.

654   *Acknowledgements.* This study was funded by the Key-Area Research and Development Program of

655   Guangdong Province (grant no. 2020B1111360003), and the Natural Science Foundation of Guangdong

656   Province (grant no. 2020A1515110526).

657

References

659   Shen, H., Liu, Y., Zhao, M., Li, J., Zhang, Y., Yang, J., Jiang, Y., Chen, T., Chen, M., Huang, X., Li, C.,

660   Guo, D., Sun, X., Xue, L., and Wang, W.: Significance of carbonyl compounds to photochemical ozone

661   formation in a coastal city (Shantou) in eastern China, Sci. Total. Environ., 764, 144031,

662   https://doi.org/10.1016/j.scitotenv.2020.144031, 2021.

663   Malley, C. S., Henze, D. K., Kuylenstierna, J. C. I., Vallack, H. W., Davila, Y., Anenberg, S. C., Turner,

664   M. C., and Ashmore, M. R.: Updated global estimates of respiratory mortality in adults ≥30 years of

665   age attributable to long-term ozone exposure, Environ. Health. Persp., 125, 087021,

666   https://doi.org/10.1289/EHP1390, 2017.

667   Avnery, S., Mauzerall, D. L., Liu, J., and Horowitz, L. W.: Global crop yield reductions due to surface

668   ozone exposure: 1. Year 2000 crop production losses and economic damage, Atmos. Environ., 45,

669   2284-2296, https://doi.org/10.1016/j.atmosenv.2010.11.045, 2011.

670   Mills, G., Sharps, K., Simpson, D., Pleijel, H., Broberg, M., Uddling, J., Jaramillo, F., Davies, W. J.,

671   Dentener, F., Van den Berg, M., Agrawal, M., Agrawal, S. B., Ainsworth, E. A., Buker, P., Emberson,

672   L., Feng, Z., Harmens, H., Hayes, F., Kobayashi, K., Paoletti, E., and Van Dingenen, R.: Ozone

673   pollution will compromise efforts to increase global wheat production, Glob. Chang. Biol., 24, 3560-

674   3574, https://doi.org/10.1111/gcb.14157, 2018.

675   Karakatsani, A., Kapitsimadis, F., Pipikou, M., Chalbot, M. C., Kavouras, I. G., Orphanidou, D., Papiris,

676   S., and Katsouyanni, K.: Ambient air pollution and respiratory health effects in mail carriers, Environ.

677   Res., 110, 278-85, https://doi.org/10.1016/j.envres.2009.11.002, 2010.

678   Berman, J. D., Fann, N., Hollingsworth, J. W., Pinkerton, K. E., Rom, W. N., Szema, A. M., Breysse, P.

679   N., White, R. H., and Curriero, F. C.: Health benefits from large-scale ozone reduction in the United

680   States, Environ. Health. Persp., 120, 1404-10, https://doi.org/10.1289/ehp.1104851, 2012.

681   O'Neill, M. S., Jerrett, M., Kawachi, I., Levy, J. I., Cohen, A. J., Gouveia, N., Wilkinson, P., Fletcher, T.,

682   Cifuentes, L., Schwartz, J.: Health, wealth, and air pollution: advancing theory and methods, Environ.

683   Health. Persp., 111, 1861-70, https://doi.org/10.1289/ehp.6334, 2003.

684   Bell, M. L., McDermott, A., Zeger, S. L., Samet, J. M., and Dominici, F.: Ozone and short-term mortality

685   in 95 US urban communities, J. Am. Med. Assoc. 1987-2000., 292, 2372-

686   2378, https://doi.org/10.1001/jama.292.19.2372, 2004.

687   Zou, Y., Deng, X. J., Zhu, D., Gong, D. C., Wang, H., Li, F., Tan, H. B., Deng, T., Mai, B. R., Liu, X. T.,

688   and Wang, B. G.: Characteristics of 1 year of observational data of VOCs, NOX and O3 at a suburban

689   site in Guangzhou, China. Atmos. Chem. Phys., 15, 6625-6636, https://doi.org/10.5194/acp-15-6625-

690   2015, 2015.

691   Zhang, A., Lin, J., Chen, W., Lin, M., and Lei, C.: Spatial-temporal distribution variation of ground-level

692   ozone in China's Pearl River Delta metropolitan region, Int. J. Environ. Res. Public Health., 18, 872,

693   https://doi.org/10.3390/ijerph 18030872, 2021.

694   Sadanaga, Y., Kawasaki, S., Tanaka, Y., Kajii, Y., and Bandow, H.: New system for measuring the

695   photochemical ozone production rate in the atmosphere, Environ. Sci. Technol., 51, 2871-2878,

696   https://doi.org/10.1021/acs.est.6b04639, 2017.

697   Cazorla, M., Brune, and W. H.: Measurement of ozone production sensor, Atmos. Meas. Tech., 3, 545-

698   555, https://doi.org/10.5194/amt-3-545-2010, 2010.

699   Lee, S.-B., Bae, G.-N., Lee, Y.-M., Moon, K.-C., and Choi, M.: Correlation between light intensity and

700   ozone formation for photochemical smog in urban air of seoul, Aerosol. Air. Qual. Res., 10, 540-549,

701   https://doi.org/10.4209/aaqr.2010.05.0036, 2010.

702   Kanaya, Y., Tanimoto, H., Yokouchi, Y., Fumikazu Taketani, F. T., Komazaki, Y., Irie, H., Takashima, H.,

703   Pan, X., Nozoe, S., and Inomata, S.: Diagnosis of photochemical ozone production rates and limiting

704   factors in continental outflow air masses reaching Fukue Island, Japan: ozone-control implications,

705   Aerosol. Air. Qual. Res., 16, 430-441, https://doi.org/10.4209/aaqr.2015.04.0220, 2016.

706   Wang, F., An, J., Li, Y., Tang, Y., Lin, J., Qu, Y., Chen, Y., Zhang, B., and Zhai, J.: Impacts of uncertainty

707   in AVOC emissions on the summer ROx budget and ozone production rate in the three most rapidly-

708   developing economic growth regions of China, Adv. Atmos. Sci., 31, 1331-1342,

709   https://doi.org/10.1007/s00376-014-3251-z, 2014.

710   Tadic, I., Crowley, J. N., Dienhart, D., Eger, P., Harder, H., Hottmann, B., Martinez, M., Parchatka, U.,

711   Paris, J.-D., Pozzer, A., Rohloff, R., Schuladen, J., Shenolikar, J., Tauer, S., Lelieveld, J., and Fischer,

712   H.: Net ozone production and its relationship to nitrogen oxides and volatile organic compounds in the

713   marine boundary layer around the Arabian Peninsula, Atmos. Chem. Phys., 20, 6769-6787,

714   https://doi.org/10.5194/acp-20-6769-2020, 2020.

715   Ren, X., van Duin, D., Cazorla, M., Chen, S., Mao, J., Zhang, L., Brune, W. H., Flynn, J. H., Grossberg,

716   N., Lefer, B. L., Rappenglück, B., Wong, K. W., Tsai, C., Stutz, J., Dibb, J. E., Thomas Jobson, B.,

717   Luke, W. T., and Kelley, P.: Atmospheric oxidation chemistry and ozone production: results from

718   SHARP   2009   in   Houston,   Texas,   J.   Geophys.   Res.-Atmos.,   118,   5770-5780,

719   https://doi.org/10.1002/jgrd.50342, 2013.

720   Lu, K., Zhang, Y., Su, H., Brauers, T., Chou, C. C., Hofzumahaus, A., Liu, S. C., Kita, K., Kondo, Y,

721   Shao, M., Wahner, A., Wang, J., Wang, X., and Zhu, T.: Oxidant (O3+ NO2) production processes and

722   formation   regimes   in   Beijing,   J.   Geophys.   Res.   Atmos.,   115,   D07303,

723   https://doi.org/10.1029/2009JD012714, 2010.

724   Zhou, W., Cohan, D. S., and Henderson, B. H.: Slower ozone production in Houston, Texas following

725   emission reductions: evidence from Texas Air Quality Studies in 2000 and 2006, Atmos. Chem. Phys.,

726   14, 2777-2788, https://doi.org/10.5194/acp-14-2777-2014, 2014.

727   Mazzuca, G. M.,Ren, X., Loughner, C. P., Estes, M., Crawford, J. H., Pickering, K. E., Weinheimer, A.

728   J., and Dickerson, R. R.: Ozone production and its sensitivity to NOx and VOCs: results from the

DISCOVER-AQ field experiment, Houston 2013, Atmos. Chem. Phys., 16, 14463-14474, https://doi.org/10.5194/acp-16-14463-2016, 2016.

Martinez, M.: OH and HO2 concentrations, sources, and loss rates during the Southern Oxidants Study in Nashville, Tennessee, summer 1999, J. Geophys. Res.-Atmos., 108, 4617, https://doi.org/10.1029/2003JD003551, 2003.

Cazorla, M., Brune, W. H., Ren, X., and Lefer, B.: Direct measurement of ozone production rates in Houston in 2009 and comparison with two estimation methods, Atmos. Chem. Phys., 12, 1203-1212, https://doi.org/10.5194/acp-12-1203-2012, 2012.

Baier, B. C., Brune, W. H., Lefer, B. L., Miller, D. O., and Martins, D. K.: Direct ozone production rate measurements and their use in assessing ozone source and receptor regions for Houston in 2013, Atmos. Environ., 114, 83-91, http://dx.doi.org/10.1016/j.atmosenv.2015.05.033, 2015.

Sklaveniti, S., Locoge, N., Stevens, P. S., Wood, E., Kundu, S., and Dusanter, S.: Development of an instrument for direct ozone production rate measurements: measurement reliability and current limitations, Atmos. Meas. Tech., 11, 741-761, https://doi.org/10.5194/amt-11-741-2018, 2018.

Liu, S. C.: Possible effects on fropospheric O3 and OH due to NO emissions, Geophys. Res. Lett., 4, 325-328, https://doi.org/10.1029/GL004i008p00325, 1977.

Pan, X.; Kanaya, Y., Tanimoto, H., Inomata, S., Wang, Z., Kudo, S., and Uno, I.: Examining the major contributors of ozone pollution in a rural area of the Yangtze River Delta region during harvest season, Atmos. Chem. Phys., 15, 6101-6111, https://doi.org/10.5194/acp-15-6101-2015, 2015.

Luecken, D. J., Phillips, S., Sarwar, and G., Jang, C.: Effects of using the CB05 vs. SAPRC99 vs. CB4 chemical mechanism on model predictions: Ozone and gas-phase photochemical precursor concentrations, Atmos. Environ., 42, 5805-5820, https://doi.org/10.1016/j.atmosenv.2007.08.056, 2008.

Zhu, M., Dong, H., Yu, F., Liao, S., Xie, Y., Liu, J., Sha, Q., Zhong, Z., Zeng, L., Zheng, J.: A new portable instrument for online measurements of formaldehyde: from ambient to mobile emission sources. Environ. Sci. Technol. Lett, 7, 292-297, https://dx.doi.org/10.1021/acs.estlett.0c00169, 2020.

Wang, C., Yuan, B., Wu, C., Wang, S., Qi, J., Wang, B., Wang, Z., Hu, W., Chen, W., Ye, C., Wang, W., Sun, Y., Wang, C., Huang, S., Song, W., Wang, X., Yang, S., Zhang, S., Xu, W., Ma, N., Zhang, Z., Jiang, B., Su, H., Cheng, Y., Wang, X., and Shao, M.: Measurements of higher alkanes using NO+

758   chemical ionization in PTR-ToF-MS: important contributions of higher alkanes to secondary organic

759   aerosols in China, Atmos. Chem. Phys., 20, 14123–14138, https://doi.org/10.5194/acp-20-14123-

760   2020, 2020a.

761   Wu, C., Wang, C., Wang, S., Wang, W., Yuan, B., Qi, J., Wang, B., Wang, H., Wang, C., Song, W., Wang,

762   X., Hu, W., Lou, S., Ye, C., Peng, Y., Wang, Z., Huangfu, Y., Xie, Y., Zhu, M., Zheng, J., Wang, X.,

763   Jiang, B., Zhang, Z., and Shao, M.: Measurement report: Important contributions of oxygenated

764   compounds to emissions and chemistry of volatile organic compounds in urban air, Atmos. Chem.

765   Phys., 20, 14769–14785, https://doi.org/10.5194/acp-20-14769-2020, 2020.

766   Yuan, B., Chen, W., Shao, M., Wang, M., Lu, S., Wang, B., Liu, Y., Chang, C.-C., and Wang, B.:

767   Measurements of ambient hydrocarbons and carbonyls in the Pearl River Delta (PRD), China, Atmos.

768   Res., 116, 93-104, https://doi.org/10.1016/j.atmosres.2012.03.006, 2012.

769   Wolfe, G. M., Marvin, M. R., Roberts, S. J., Travis, K. R., and Liao, J.: The Framework for 0-D

770   Atmospheric Modeling (F0AM) v3.1, Geosci. Model. Dev., 9, 3309-3319,

771   https://doi.org/10.5194/gmd-9-3309-2016, 2016.

772   Jenkin, M. E., Young, J. C., and Rickard, A. R.: The MCM v3.3.1 degradation scheme for isoprene,

773   Atmos. Chem. Phys., 15, 11433-11459, https://doi.org/10.5194/acp-15-11433-2015, 2015.

774   Liu, X., Wang, N., Lyu, X., Zeren, Y., Jiang, F., Wang, X., Zou, S., Ling, Z., and Guo, H.: Photochemistry

775   of ozone pollution in autumn in Pearl River Estuary, South China, Sci. Total Environ., 754, 141812,

776   https://doi.org/10.1016/j.scitotenv.2020.141812, 2020.